Journal of Solid State Chemistry 348 (2025) 125328

Contents lists available at ScienceDirect

Journal of Solid State Chemistry

journal homepage: www.elsevier.com/locate/jssc

# Crystal structure, spectroscopy, and magnetism of alternating trinuclear, bridged hydroxo and oxo copper (II) complexes

Marcel Hirrle [a], Richard Röß-Ohlenroth [a], Tobias Luxenhofer [a], Björn Bredenkötter [a], Maryana Kraft [a], Hans-Albrecht Krug von Nidda [b], Dirk Volkmer [a,*]

[a] Institute of Physics, University of Augsburg, Universitätsstraße 1, D-86159, Augsburg, Germany
[b] Experimental Physics V, Center for Electronic Correlations and Magnetism, Institute of Physics, University of Augsburg, Universitätsstraße 1, D-86159, Augsburg, Germany

A B S T R A C T

The synthesis, structure, and magnetic properties of a novel metal-organic framework (MOF), **CFA-24** ($[Cu_6(dmta)_9O(OH)]$; **H-dmta** = 4,5-Dimethyl-1*H*-1,2,3-triazole), featuring alternating oxo- and hydroxo-bridged Cu (II) triangles are the focus of this study. The synthesis process of **H-dmta** and **CFA-24** was optimized to ensure scalability and high yields, with the resulting MOF characterized using single-crystal X-ray diffraction, powder X-ray diffraction, thermogravimetric analysis, and various spectroscopic techniques. Structural analysis revealed a chiral cubic crystal system (space group $P2_13$), with copper ions forming equilateral triangles linked by triazoles. The study also explores the magnetic behaviour of **CFA-24** using SQUID magnetometry and theoretical modeling. The magnetic data indicate strong antiferromagnetic interactions, modulated by Dzyaloshinskii-Moriya interactions (DMI), which contribute to the system's complex magnetic ground state. This research enhances the understanding of magnetically frustrated systems and positions **CFA-24** as a potential candidate for spintronic applications.

## 1. Introduction

The distinctive structural diversity and flexible porosity of metal-organic frameworks (MOFs) present unique opportunities for the integration of magnetic functionalities [1]. As hybrid materials composed of inorganic nodes and organic linkers, MOFs allow for the precise design of magnetic properties [2] and enable the coupling of these functionalities with other physical characteristics [3–10].

In 2012, research on MOFs comprised of 1*H*-1,2,3-triazole (**H-ta**) ligands started, resulting in $Cu(ta)_2$, which is composed of condensed Kuratowski units [11] that are Jahn-Teller distorted. $Cu(ta)_2$ was studied for its magnetic properties displaying a partial frustration of the copper ions [12]. To gain deeper insights into the magnetic properties similar Kuratowski complexes [13] were synthesized in 2016 to minimize the interaction between the units, exhibiting weak anti-ferromagnetic exchange. Driven by these results, further research was carried out with other metals and the simple **H-ta** linker. Thereof, the iron derivative $[Fe(ta)_2]$ [14], which displays the largest known hysteresis due to a cooperative spin-crossover (SCO) at elevated temperatures, as well as the frustration observed in the centered pyrochlore lattice of $[Mn(ta)_2]$[47] should be highlighted. A deeper analysis of $[Mn(ta)_2]$ predicted that it displays distinct features of a classical spin liquid with a structure factor reflecting Coulomb physics in the presence of charges. By switching the metal ion to Chromium [15] the magnetic behaviour could be turned into ferromagnetic with a Curie temperature of 225 K and a large negative magnetoresistance at 5 K could be achieved. Starting from $[Fe(ta)_2]$ we tried to influence the SCO by making small changes to the organic linker. The steric change caused by the addition of organic groups to the **H-ta** linker resulted in a shift of the spin crossover to lower temperatures.

Similar attempts were conducted with copper and 4,5-dimethyl-1H-1,2,3-triazole (H-dmta) as a ligand. However, these attempts did not yield Kuratowski-type secondary building units. Instead, they resulted in the formation of equilateral and interconnected copper triangles. These are of great interest to those working in the field of magneto chemistry, as they can demonstrate the behaviour of magnetically frustrated systems [16]. The frustration in those triangles arises from the geometry or topology of the lattice. Frustration means that the system cannot satisfy all exchange interaction at the same time, this leads to interesting ground states which can have a large degeneracy. To explain the behaviour of such systems more than the isotropic exchange is needed. The missing component, the antisymmetric exchange (ASE) can be described as $G_{ij} = [S_i \times S_j]$ which was first introduced phenomenologically by Dzyaloshinskii to describe the weak ferromagnetism in $Fe_2O_3$ [17]. Later Moriya defined the microscopic explanation of G [18]. To honour both contributions, the ASE is also called the

* Corresponding author.
*E-mail address:* dirk.volkmer@physik.uni-augsburg.de (D. Volkmer).

https://doi.org/10.1016/j.jssc.2025.125328
Received 13 February 2025; Received in revised form 7 March 2025; Accepted 17 March 2025
Available online 25 March 2025

Dzyaloshinskii-Moriya interaction (DMI).

$[Cu_3^{II}]$ triangles are the best examples to observe DMI, since they offer the simplest way to display equilateral triangles with antiferromagnetic exchange. Surprisingly, there is a lack of comprehensive information regarding the G value in those complexes. With our new MOF we want to dig deeper and provide more insight into this phenomenon.

Therefore, preparation procedures for the novel **CFA-24** ([$Cu_6$(dmta)$_9$O(OH)]; H-dmta = 4,5-dimethyl-1*H*-1,2,3-triazole) metal-organic framework, which features alternating oxo- and hydroxo-bridged Cu (II) triangles interconnected in 3 dimensions, were optimized and a facile and scalable synthesis route was adapted from literature procedures to obtain the 4,5-dimethyl-1*H*-1,2,3-triazole (**H-dmta**) in good yields. The resulting MOF structure was characterized by single-crystal X-ray diffraction (SC-XRD), powder X-ray diffraction (PXRD), variable-temperature PXRD (VT-PXRD), thermogravimetric analysis (TGA), argon adsorption, attenuated total reflectance Fourier transform infrared spectroscopy (ATR-FT-IR), diffuse reflectance Fourier transform infrared spectroscopy (DRIFTS). To deepen the understanding of the magnetic properties of the framework, electron spin resonance (ESR) as well as magnetic susceptibility and magnetization measurements in conjunction with simulations were applied.

## 2. Experimental section

### 2.1. Materials

Ethanol (99.8 % analytical grade; VWR), methanol (99.8 % analytical grade; VWR), ammonia solution (25 % technical grade, VWR), and copper(II)hydroxide (technical grade, Sigma-Aldrich) were used as received from the commercial supplier.

**Attenuated total reflectance (ATR) and diffuse-reflectance Fourier transform (DRIFT) infrared spectroscopy.** Fourier transform infrared (FT-IR) spectra were recorded in the range of 4000–400 $cm^{-1}$ with a Bruker Equinox 55 FT-IR spectrometer equipped with the PLATINUM ATR unit and a KBr beam splitter. The diffuse-reflectance infrared Fourier transform (DRIFT) spectra were measured with a Harrick praying mantis reaction chamber in the range of 4000–400 $cm^{-1}$ on the same instrument with KBr as a reference. The powdered KBr background was heated at 300 °C in a nitrogen gas stream prior to the measurement and sample mounting. The sample was directly dispersed into the KBr background without prior mixing and grinding. Each spectrum was obtained as the accumulation of 32 scans with a 4 $cm^{-1}$ resolution. The signals were labelled as strong (s), medium (m), weak (w), and broad (br).

**Thermogravimetric analysis.** A TA Instruments Q500 thermogravimetric analyser was used to obtain the thermogravimetric analysis (TGA) data, which was recorded after a 5 min isothermal step in the temperature range of 25–700 °C with a heating rate of 10 $Kmin^{-1}$ under a nitrogen gas stream.

**Argon adsorption measurements.** The argon adsorption isotherm of a sample activated at 120 °C for 1 h was acquired with a Quantachrome Autosorb-I ASI-CP-8 instrument at 77.3 K in the range of $5.00 \times 10^{-5} \leq p/p_0 \leq 1.00$. The resulting Brunauer–Emmett–Teller (BET) specific surface area was calculated with consideration of the criteria proposed by Rouquerol et al. [19] A nonlocal density functional theory (NLDFT) pore size distribution was gained using a carbon equilibrium kernel based on a slit pore model for argon adsorption at 77 K in the Autosorb-1 software [20].

**Scanning electron microscopy (SEM).** SEM micrographs were recorded on a Zeiss Crossbeam 550 scanning electron microscope.

**Powder X-Ray diffraction (PXRD).** The PXRD and VT-PXRD patterns were collected with a Malvern Panalytical Empyrean diffractometer equipped with a Bragg–Brentano$^{HD}$ mirror, a PIXcel$^{3D}$ 2 × 2 detector, and a XRK 900 reactor chamber with 0.026° steps and a measurement time of 1595 s for each pattern in the range of 3–50° 2θ. The samples were heated with 25 °C steps up to 300 °C and in 50 °C steps up to 500 °C with a 5 °C/min heating rate under nitrogen atmosphere.

**Nuclear magnetic resonance (NMR) spectroscopy.** $^1H$ nuclear magnetic resonance (400 MHz) and $^{13}C$ NMR (100 MHz) spectra were obtained by a BRUKER-Avance EVO 400 and the chemical shifts were reported in ppm relative to the solvent signal.

**Single-crystal X-ray diffraction and structure refinement.** Single-crystal X-ray diffraction data set was collected with a Bruker D8 Venture diffractometer equipped with a low-temperature device at 101(2) K. APEX4 (v2021.10–0) software [21] was used for collecting, initial indexing and processing of the intensities. The raw data frames were integrated and corrected for absorption effects using the Bruker SAINT [22] and SADABS [23] software packages. The structures were solved and refined using the Bruker SHELXTL Software Package [24]. All non-hydrogen atoms were refined anisotropically. The disorder of the hydroxo-group was refined with occupancies 0.885/0.115 over two sides of the $Cu_3$-building unit. The position of hydrogen atom of the OH-group with the main occupancy was determined from the difference Fourier map and fixed at the O–H distance 0.82 Å. All other H atoms were positioned geometrically and constrained to ride on their parent atoms. It was not possible to refine the solvent molecules in the voids; hence, the SQUEEZE [25] procedure was applied to the data. Selected crystal data and the refinement details are listed in Table 1. Complete crystallographic data for the structures reported in this paper can be obtained from the Cambridge Crystallographic Data Centre as supplementary publication no. CCDC 2391495.

### 2.2. Magnetic measurements

ESR measurements were performed in a continuous wave spectrometer (Bruker ELEXSYS E500) at $\nu = 9.35$ GHz in the temperature region $4 \leq T \leq 300$ K using a continuous He gas-flow cryostat (Oxford Instruments).

Magnetic susceptibility and magnetization measurements were performed using a superconducting quantum interference device (SQUID) magnetometer (Quantum Design, MPMS5) working in the temperature range of $1.8 \leq T \leq 400$ K in magnetic fields up to 5 T.

### 2.3. Syntheses

4,5-Dimethyl-1*H*-1,2,3-triazole (**H-dmta**) was synthesized from butane-2,3-dione in a three-step synthesis. 2,3-Butanedihydrazone (**1**) was prepared according to the literature procedure [26]; the subsequent steps, ring-closure and deamination, were adapted from literature procedure [27] und [28] (see Fig. Scheme 1).

2,3-Butanedihydrazone (**1**) [22]:

To a solution of hydrazine-monohydrate (9.7 mL, 0.2 mol) (Alfa

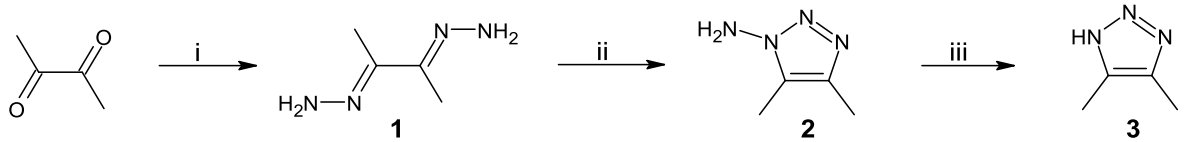


**Scheme 1.** Synthesis of 4,5-dimethyl-1*H*-1,2,3-triazole (**H-dmta**); i) $H_2NNH_2{\cdot}H_2O$, EtOH, reflux, 2h, 90 %; ii) $MnO_2$, $CHCl_3$, r.t., 2.5 h, 79 %; iii) $NaNO_2$, $AcOH/H_2O$, r.t., 2 h, 77 %.

**Table 1**
Crystal data and structure refinement for **CFA-24**.

| | | |
|---|---|---|
| Empirical formula | $C_{36}H_{55}Cu_6N_{27}O_2$ | |
| Formula weight [gmol$^{-1}$] | 1279.31 | |
| Temperature [K] | 101(2) | |
| Wavelength [Å] | 0.71073 | |
| Crystal system | Cubic | |
| Space group | $P2_13$ | |
| Unit cell dimensions [Å] | a = 18.4800(5) Å | α = 90°. |
| | b = 18.4800(5) Å | β = 90°. |
| | c = 18.4800(5) Å | γ = 90°. |
| Volume [Å$^3$] | 6311.1(5) | |
| Z | 4 | |
| Density (calculated) [gcm$^{-3}$] | 1.346 | |
| Absorption coefficient [mm$^{-1}$] | 2.036 | |
| F(000) | 2600 | |
| Crystal size [mm$^3$] | 0.12 × 0.08 x 0.08 | |
| Theta range for data collection [°] | 2.204 to 29.998 | |
| Index ranges | −26 ≤ h<=26, −26 ≤ k<=26, −26 ≤ l<=26 | |
| Reflections collected | 467927 | |
| Independent reflections | 6133 [R(int) = 0.0748] | |
| Completeness to theta = 25.242° [%] | 99.6 | |
| Absorption correction | Semi-empirical from equivalents | |
| Max. and min. transmission | 0.7329 and 0.6955 | |
| Refinement method | Full-matrix least-squares on $F^2$ | |
| Data/restraints/parameters | 6133/13/225 | |
| Goodness-of-fit on F2 | 1.145 | |
| Final R indices [I > 2sigma(I)] | R1 = 0.0297, w*R*2 = 0.0888 | |
| R indices (all data) | R1 = 0.0317, w*R*2 = 0.0910 | |
| Absolute structure parameter | 0.013(4) | |
| Largest diff. peak and hole [e. Å$^{-3}$] | 0.595 and −0.463 | |

Aesar, 100 %) in EtOH (20 mL) butane-2,3-dione (8.6 mL, 0.1 mol) was added dropwise and the resulting solution was refluxed for 2 h. After cooling to room temperature, the precipitated colourless needles were filtered, washed with EtOH and dried in vacuum to yield analytically pure 10.2 g (0.18 mol, 90 %) (**1**).

FTIR (Wavenumber in cm$^{-1}$): 3331, 3186, 1635, 1572, 1456, 1361, 1277, 1125, 1081, 939, 698, 664, 455.

$^1$H NMR (400 MHz, DMSO-$d_6$): δ = 6.13 (s, 4H, $NH_2$), 1.80 (s, 6H, $CH_3$) ppm.

4,5-Dimethyl-1*H*-1,2,3-triazol-1-amine (**2**):

To a solution of 2,3-butanedihydrazone (**1**) (2.28 g, 20.0 mmol) in chloroform (100 mL) activated $MnO_2$ (8.7 g,0.1 mol) was added and the mixture was stirred vigorously for 2.5 h $MnO_2$ was removed by filtration over Celite, the solvent was evaporated and the residue was dried under vacuum to yield 1.76 g (15.7 mmol, 79 %) (**2**) as a light-yellow solid, which was used in the next step without further purification.

FTIR (Figure S1) (Wavenumber in cm-1): 3271 (s), 3130 (br,s), 2974 (m), 1703 (br, w), 1637 (m), 1588 (m), 1444 (m), 1385 (m), 1355 (m), 1255 (s), 1221 (m), 1183 (m), 1133 (m), 1033 (w), 991 (s), 953 (w), 776 (m), 715 (s), 590 (w), 508 (br,s), 453 (br,w).

$^1$H NMR (400 MHz, DMSO-$d_6$): δ = 6.59 (s, 2H, $NH_2$), 2.12 (s, 6H, $CH_3$) ppm.

4,5-Dimethyl-1*H*-1,2,3-triazole (**H-dmta**):

To a solution of 4,5-dimethyl-1*H*-1,2,3-triazol-1-amine (**2**) (1.68 g, 15 mmol) in acetic acid (30 mL) sodium nitrite (1.56 g, 22.5 mmol) dissolved in water (15 mL) was added dropwise. The mixture was stirred for 2 h, diluted with water (75 mL) and neutralized with saturated sodium hydrogen carbonate solution (100 mL). The resulting solution was extracted with diethyl ether in a rotation perforator for 15 h. The solvent was dried over $Na_2SO_4$ and evaporated to give pure **H-dmta** (1,10 g, 11,3 mmol, 77 %) as a colourless solid. Ultrapure **H-dmta** can be obtained by sublimation (65 °C), 0,01 mbar).

Melting Point: 70 °C.

FT-IR (Fig. S2) (Wavenumber in cm$^{-1}$): 3346 (br), 3172 (w), 3115 (w), 3030 (w), 2931 (w), 2754 (w), 2719 (w), 1880 (br,w), 1668 (w), 1600 (m), 1513 (w), 1441 (br), 1388 (w), 1296 (w), 1225 (m), 1192 (w), 1132 (s), 1028 (m), 958 (br,s), 715 (m), 669 (w), 610 (br,s), 419 (m).

$^1$H NMR (Fig. S3) (400 MHz, DMSO-$d_6$): δ = 13.8–14.8 (br, 1H, NH), 2.15 (s, 6H, $CH_3$) ppm.

$^{13}$C NMR (Fig. S4) (400 MHz, DMSO-$6_6$): δ = 140.67, 9.77 ppm.

Single-crystal synthesis of $Cu_6$(dmta)$_9$O(OH) (**CFA-24**):

$Cu(OH)_2$ (11.2 mg, 0.11 mmol) dissolved in ammonia solution (2 mL, 25 %) and a solution of 4,5-dimethyl-1*H*-1,2,3-triazole (**dmta**) (40 mg, 0.41 mmol) in ethanol (1 mL) were mixed in a pyrex sample tube, partially sealed with a screw cap, and heated in a heating block at 120 °C for 24 h. The resulting dry green crystals were measured without further treatment.

Bulk synthesis of $Cu_6$(dmta)$_9$O(OH) (**CFA-24**):

In a 50 mL round bottom flask equipped with a small reflux condenser $Cu(OH)_2$ (56 mg, 0.57 mmol) was dissolved in ammonia solution (10 mL, 25 %) and a solution 4,5-dimethyl-1*H*-1,2,3-triazole (**dmta**) (200 mg, 2.06 mmol) dissolved in ethanol (5 mL) was added. The resulting solution was stirred under reflux conditions at 90 °C for 24 h. Filtration and washing of the precipitate with ethanol (2 × 10 mL) and methanol (2 × 10 mL) afforded the product as a green powder after drying in vacuum for 24 h (123 mg, 93 % based on $Cu(OH)_2$).

FT-IR (Fig. S5) (Wavenumber in cm$^{-1}$): 2920 (m), 2862 (w), 1637 (w), 1548 (m), 1438 (m), 1385 (m), 1313 (w), 1239 (s), 1217 (s), 1200 (w), 1018 (w), 736 (s), 654 (s), 582 (s), 428 (s).

## 3. Results and discussion

### 3.1. Synthesis

4,5-Dimethyl-1*H*-1,2,3-triazole (**H-dmta**) was synthesized from butane-2,3-dione in a scalable three-step synthesis in good yields. First butane-2,3-dione was reacted in a condensation reaction with hydrazine to 2,3-butanedihydrazone (**1**) [26].

In the second step the bishydrazone (**1**) was oxidized with $MnO_2$ in chloroform, and the intermediate diazohydrazone undergoes ring closure to form 4,5-dimethyl-1*H*-1,2,3-triazol-1-amine (**2**) [27] which was deaminated with $NaNO_2$ in acidic acid to give 4,5-dimethyl-1*H*-1,2,3-triazole (**H-dmta**).

Green single-crystals of the novel $Cu_6$(dmta)$_9$O(OH) (**CFA-24**) framework were obtained by reactions in screw-cap test tubes (Fig. S6). The synthesis of **CFA-24** was further improved with a bulk material synthesis under reflux conditions to obtain larger amounts of the pure phase compound with good yields.

### 3.2. Characterization

The PXRD pattern of the bulk **CFA-24** shows a good match with the pattern calculated from the single-crystal structure determination (Fig. S7), thus, verifying the phase purity of the material. Argon adsorption isotherms (Fig. S8) of the sample resulted in a BET surface area of 724 $m^2g^{-1}$ (Fig. S9) and a pore size distribution (Fig. S10), which are both in good agreement with the observed structure. The thermal stability of **CFA-24** was investigated with VT-PXRD (Fig. S11) measurements, showing a decrease of crystallinity at 200 °C and a complete loss of crystallinity at 225 °C, which coincides well with the first large weight loss step starting at 200 °C in the TGA curve (Fig. S12). The centering via central hydroxy groups in the trinuclear SBUs, which was only indirectly suggested from the Cu(II)–O distances from the single-crystal structure and due to charge balance, could be confirmed by the DRIFT spectrum of activated **CFA-24** showing the symmetric O–H stretching vibration at 3596 cm$^{-1}$ (Fig. S13).

### 3.3. Structural description of the $Cu_6$(dmta)$_9$O(OH) MOF

The structure of **CFA-24** was determined by single crystal X-ray

analysis. The detailed crystallographic data including the bond distances and angles are shown in the supporting information. The compound crystallises in the cubic chiral space group $P2_13$ (198). The asymmetric unit, shown in Fig. S14 in the Ortep style, consists of 2 copper atoms, their associated oxo- or hydroxo-centering oxygen and 3 dmta units.

**CFA-24** is constructed from two types of secondary building units (SBUs) – $[Cu_3(\mu_3\text{-}O)dmta_3]^+$ and $[Cu_3(\mu_3\text{-}OH)dmta_3]^{2+}$. Within each SBU three copper ions build an equilateral triangle building unit either with hydroxo- or oxocentering and three $dmta^-$ groups acting as the triangle edges (Fig. 1a). Tricopper structure building units are a coordination motif frequently observed in pyrazolates, pyridinates, and amidinates of low-valent metals [29]. The intracluster Cu–Cu and Cu–O distances in **CFA-24** increase from 3.2728(5) Å and 1.9097(7) Å in oxocentered to 3.4327(5) Å and 2.0201(13) Å in hydroxocentered $Cu_3$-building unit respectively. These distances are close to those in $Cu_3(\mu_3\text{-}O)$ and $Cu_3(\mu_3\text{-}OH)$ clusters reported by Angaridis and Rivera-Carrillo [30,31]. Both $Cu_3(\mu_3\text{-}O)$ and $Cu_3(\mu_3\text{-}OH)$ moieties show deviation from planarity with a $Cu_3$-plane–O1 distance of 0.277 Å in $Cu_3(\mu_3\text{-}O)$ and 0.392 Å in $Cu_3(\mu_3\text{-}OH)$. The $Cu_3(\mu_3\text{-}OH)$ demonstrates a disorder with occupancy of two different coordination sites with an occupation ration of 88.5 %–11.5 %, whereas CuO exhibits no such discrepancy. Each copper atom has a distorted square pyramidal coordination, showing a tendency towards a trigonal-bipyramidal coordination geometry shown by the geometry parameter τ of 0.53, by four nitrogen atoms of neighbouring dmta-groups and one oxygen (Fig. 1). While for Cu1 all distances are close to each other and range from 1.964 (3) Å to 2.109(3) Å, one longer Cu2–N3 contact of 2.324(3) Å is observed between Cu2 and the N-atom of the dmta-group of the neighbouring SBU. The atomic coordinates, isotropic thermal parameters, selected bond lengths and angles for **CFA-24** are given in Table S3.

The SBUs are interconnected via common deprotonated $dmta^-$ ligands (Fig. 1b) forming a three-dimensional coordination network. This network is outlined in a simplified manner in Fig. 2b by representing the $Cu_3(\mu_3\text{-}O)$ and $Cu_3(\mu_3\text{-}OH)$ moieties as red and blue triangles, respectively (Fig. 2a). Potential solvent-accessible void volume of 1957 $Å^3$ (31.0 % of the unit cell volume of 6311.1(5) $Å^3$) was calculated with PLATON/SQUEEZE [25] software for **CFA-24**. According to the calculated 380 electron counts/cell, the voids should be occupied by ethanol, water, and/or ammonia molecules used as solvents in the synthesis. The **CFA-24** coordination network can also be described as a network comprising (10,3)-a topology (type srs, $SrSi_2$) by regarding the $Cu_3O/OH$ building units as three-connected nodes and neglecting the two-coordinated dmta moieties (see Fig. 2c). This representation clearly highlights that helical chains are running along the *c*-direction of the structure, which is consistent with the chirality of **CFA-24**.

### 3.4. Magnetic properties

Magnetic susceptibility measurements of the polycrystalline sample were performed in a magnetic field of 1000 Oe for temperatures between 1.8 and 400 K. The temperature dependence of the molar susceptibility $\chi_m(T)$, the product $\chi_m T$ $(T)$, and the inverse molar susceptibility $\chi_m^{-1}(T)$ is shown in Fig. 3.

Starting from high temperature, the susceptibility $\chi_m(T)$ of both compounds increases gradually on decreasing temperature and diverges at low temperatures. The $\chi_m^{-1}(T)$ behaviour can be divided into two different regimes. In the high temperature regime, above room temperature, it follows a Curie-Weiss law with a Curie constant $C_{hT}$=2.87 emu $mol^{-1}$ K. This is slightly above the spin only value for 6 uncoupled spin ½ ($C_{theo}$ = 2.48 assuming g = 2). The resulting g = 2.15 is typical for $Cu^{2+}$ ions in octahedral ligand field with nearly quenched orbital contributions [32]. The Curie temperature Θ = −440 K clearly indicates a strong antiferromagnetic behaviour. In the low temperature regime, below 50 K, the susceptibility also follows a Curie-Weiss law but with $C_{lT}$ = 0.77 emu $mol^{-1}$ K, which indicates that only 2 spins are still visible, and the rest of the spins is paired off. The Θ = −15 K of those remaining spin is slightly antiferromagnetic.

The product $\chi_m T$ $(T)$ declines steadily with decreasing temperature until it drops drastically around 70 K towards zero. Around room temperature $\chi_m T$ (300 K) = 1.165 emu K/mol is appreciably lower than the value expected for 6 uncoupled S = ½ spins (2.25 emu K/mol g = 2). This also hints to a strong antiferromagnetic exchange. At around 100 K $\chi_m T$ (100 K) = 0.74 emu K/mol corresponds to 2 uncoupled S = ½ spins (0.75 emu K/mol g = 2), which fits to 1 copper ion per triangle. The drop to even lower values can be explained by the incorporation of Dzyaloshinskii-Moriya interaction (DMI) and the pairing of the triangles.

Magnetization curves $M(H)$ of the sample were measured in magnetic fields $H$ up to 5 T at temperatures of 1.8, 5, and 10 K as shown in Fig. 4.

The magnetization reveals no saturation behaviour at any temperature. Surprisingly, the magnetization for 1.8 K and 5 K is almost on top of each other. The absence of the saturation behaviour indicates the presence of very strong antiferromagnetic exchange coupling between the spins as also seen in the susceptibility measurements.

X-band ESR measurements were performed to gain further insights into the magnetic properties of **CFA-24**. Unfortunately, the sample was silent over the whole temperature range from 4 to 300 K. Similar observations were already reported in literature and explained by strong interactions and a fast electron spin relaxation [30,33,34].

Since no conclusions could be drawn from the ESR measurement, the magnetic behaviour was analysed using the program PHI [35] to fit the molar susceptibility and magnetization data with a molecular approach

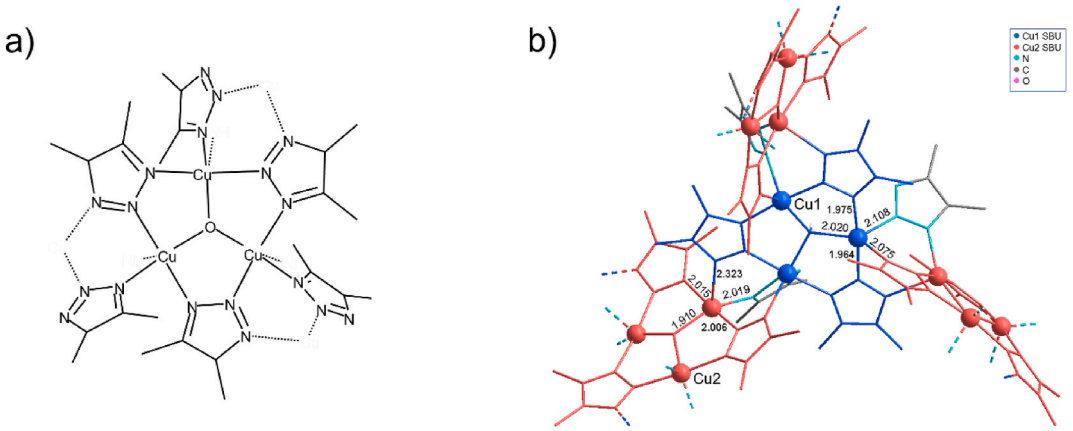


**Fig. 1.** (a) Coordination unit with trinuclear Cu(II)-centers. (b) Coordination network of **CFA-24** with highlighted SBUs and copper coordination.

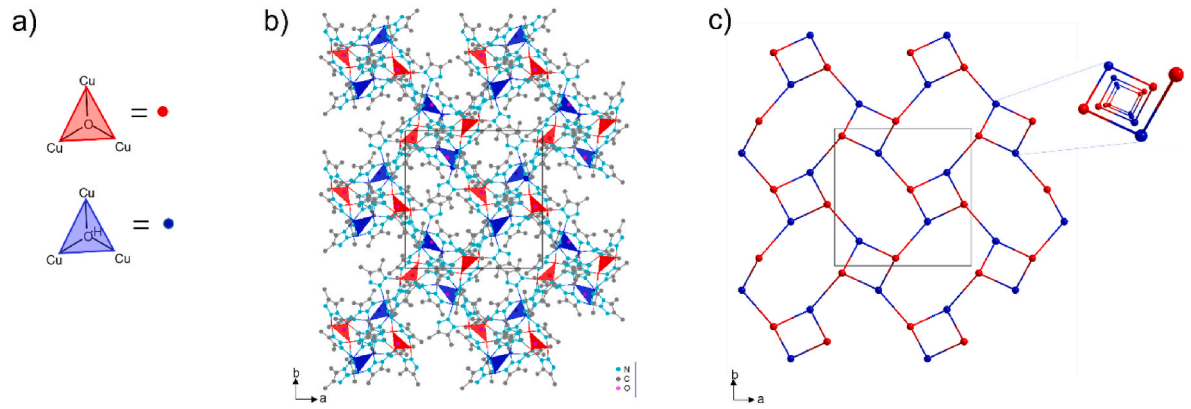


**Fig. 2.** (a) Representation of $Cu_3(\mu_3\text{-}O)$ and $Cu_3(\mu_3\text{-}OH)$ structure building units on b) and c) diagrams. (b) Packing diagram of **CFA-24** with highlighted tricopper building units showing porous 3D framework projected along the c-axis. (c) Topologic representation of **CFA-24** showing a (10,3)-a or srs type network and the helical chains running along the c-axis.

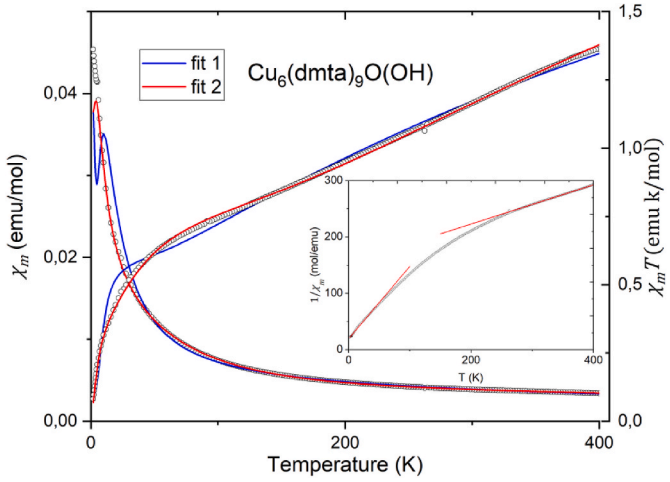


**Fig. 3.** Temperature dependence of the molar susceptibility $\chi_m(T)$ and product $\chi_mT(T)$ at 1000 Oe. Open symbols show the experimental data, the error for the susceptibility calculated from TIP, which includes all relevant influences, is around the size of the symbols. Blue solid lines represent fits (fit 1) based on the model Hamiltonian $\hat{H}_1$. Red solid lines represent fits (fit 2) based on the ASE Hamiltonian $\hat{H}_2$. Both models are given in the text. Inset: Inverse molar susceptibilities $1/\chi_m(T)$ fitted with 2 Ci Weiss laws for the different temperature regimes.

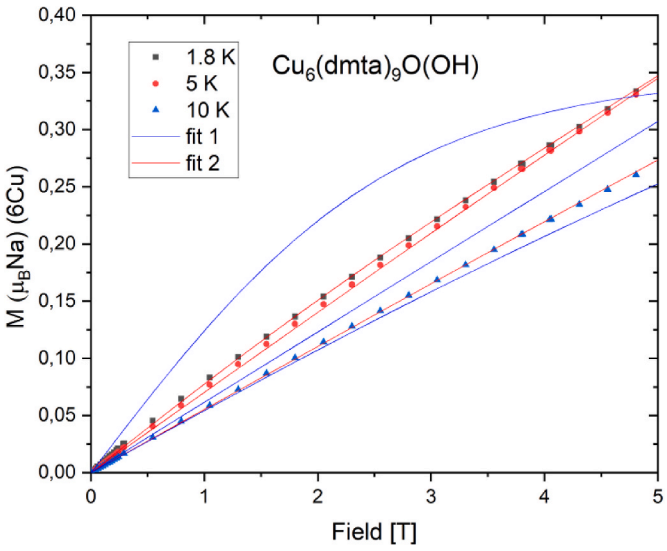


**Fig. 4.** Field-dependent magnetization curves M(H) at 1.8, 5 and 10 K. Open symbols show the experimental data, blue solid lines represent fits (fit 1) based on the model Hamiltonian $\hat{H}_1$. Red solid lines represent fits (fit 2) based on the ASE Hamiltonian $\hat{H}_2$. Both models are given in the text.

for exchange-coupled Cu(II) ions. In general, the exchange interactions and g-factors must be treated as tensors, and their spatial orientation must be considered in the calculation. However, as we measured a polycrystalline material, the anisotropies are averaged out. Therefore, the fit parameters could be reduced to the following isotropic Heisenberg–Dirac–van Vleck (HDVV) spin Hamiltonian for the exchange coupling combined with terms for the Zeeman splitting in the external magnetic field $\vec{H}$. In the following formula we use the notation: exchange coupling J as shown in Fig. 5, spin S, g-factor g and μB Bohr magneton.

$$\hat{H}_1 = -2\sum_{i=1,j>i}^{3} J_1\,\vec{S}_i\vec{S}_j - 2\sum_{i=4,j>i}^{6} J_3\,\vec{S}_i\vec{S}_j - 2\sum_{i=3,j>i}^{4} J_2\,\vec{S}_i\vec{S}_j + g^*\mu_B\sum_{i=1}^{6}\vec{S}_i{}^*\vec{H}$$

This model (fit1) can provide a rough estimate of the exchange parameters from the high temperature susceptibility ($J_1 = -56$ cm$^{-1}$, $J_2 = -151$ cm$^{-1}$, $J_3 = -14$ cm$^{-1}$, TIP = 1.19e-3 cm$^3$mol$^{-1}$). At low temperatures, this approach is not sufficient because small deviations in the susceptibility become visible, and the magnetization cannot be reproduced Fig. 5.

The initial model was selected based on its structural characteristics, as determined by the crystal structure, which revealed that copper atoms form two distinctively bridged equilateral triangles. We expected different strengths due to the bridges, thus two exchange parameters $J_1$ and $J_2$ were introduced. These triangles are connected via N–N bridges which is included with parameter $J_3$.

The introduction of antisymmetric exchange (ASE) (fit 2) for each triangle, the fitting works over the entire temperature range and reproduces the magnetization perfectly. Each triangle received DMI in a different direction because they are rotated with respect to each other. The other directions were assumed to be 0 due to the behaviour of an equilateral triangle [36]. This could not be verified because the equation would be overparameterized.

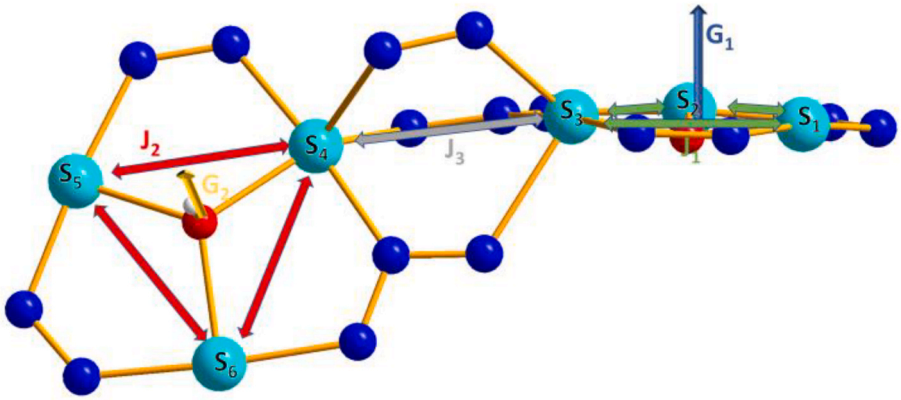


**Fig. 5.** Representation of $Cu_6(dmta)_9O(OH)$ MOF as a bis-triangular system. The isotropic exchange is shown in two-headed arrows (red, grey and green) and the antisymmetric exchange is shown in orange and blue showing the need of two different ASE directions.

$$\widehat{H}_2 = -2\sum_{i=1j>i}^{3} J_1\,\vec{S}_i\vec{S}_j - 2\sum_{i=4j>i}^{6} J_3\,\vec{S}_i\vec{S}_j - 2\sum_{i=3j>i}^{4} J_2\,\vec{S}_i\vec{S}_j + g^*\mu_B \sum_{i=1}^{6}\vec{S}_i{}^*\vec{H} + G_1\left(\vec{S}_1\times\vec{S}_2 + \vec{S}_2\times\vec{S}_3 + \vec{S}_3\times\vec{S}_1\right) + G_2\left(\vec{S}_4\times\vec{S}_5 + \vec{S}_5\times\vec{S}_6 + \vec{S}_6\times\vec{S}_4\right)$$

with the constants as described before and G as the antisymmetric vector.

The improved model yields slightly higher values $J_1 = -198\ cm^{-1}$, $J_2 = -124\ cm^{-1}$, $J_3 = -15\ cm^{-1}$, $DMI_1 = -64\ cm^{-1}$, $DMI_2 = -80\ cm^{-1}$, TIP = 0.68e-3 $cm^3mol^{-1}$. It is notable that only the parameters to which the DMI was added underwent a change, whereas the exchange for linking the two triangles together remained unaltered. From Zeeman second order perturbation theory it is possible to calculate the theoretical TIP which is 60e-6 $cm^3mol^{-1}$ per copper ion. Therefore, our fit results are in reasonable agreement with 3.6e-4 $cm^3mol^{-1}$ for 6 copper ions. For deeper investigation single crystal measurements would be necessary [37–39] and maybe NMR measurements.

Concluding from the comparison with literature we assigned the stronger exchange to the OXO-bridged triangle and the weaker exchange to the HYDROXO-bridged triangle. In comparison to other copper triangles (see Table 2), our OXO exchange is situated in the midrange, while the HYDROXO exchange is positioned at the lower end.

The major difference is in the strength of the DMI. Not many have calculated the DMI and if, they are usually weaker in absolute values. Indeed, one has to compare the ratio of anisotropic vs. isotropic exchange DMI/J. In this respect our values ($DMI_1/J_1 = 0.32$ and $DMI_2/J_2 = 0.64$) are comparable to others found in other Triangular Tricopper(II) Complexes as seen in Refs. [36,45]. Note that compared to the original materials, i.e. transition metal oxides like $\alpha$-$Fe_2O_3$ and $MnCO_3$, where DMI was found as in Refs. [17,46], our exchanges are larger by up to a factor of 10.

**Table 2**
Selected magneto-structural data of different $Cu_3O$ and $Cu_3OH$ systems.

| Compound | Cu …. Cu (Å) | -J ($cm^{-1}$) | Ref. |
|---|---|---|---|
| $Cu_6(dmta)_9O(OH)$ | 3.450 | 124 | this work |
| $Cu_6(dmta)_9O(OH)$ | 3.277 | 198 | this work |
| $[Cu_3(OH)(aat)_3(CF_3SO_3)(H_2O)](CF_3SO_3)$ | 3.355 | 197.7 | [40] |
| $[Cu_3(OH)(aat)_3(NO_3)(H_2O)_2](NO_3)\cdot(H_2O)_2$ | 3.341 | 190.9 | [40] |
| $[Cu_3(OH)(aat)_3(ClO_4)(H_2O)_2](ClO_4)$ | 3.371 | 198.2 | [40] |
| $[Cu_3(trz)_3(OH)][Cu_2Br_4]$ | 3.502 | 180 | [41] |
| $[Cu_3(OH)(aaat)_3(H_2O)_3](NO_3)_2\cdot H_2O$ | 3.347–3.393 | 195 | [42] |
| $[\{Cu_3(OH)(pz)_3(Hpz)_3\}_2SO_4](NO_3)_2\cdot MeCN\cdot MeOH\cdot 1.5H_2O$ | 3.182–3.354 | 180 | [43] |
| $[PPN]_2[Cu_3(\mu_3\text{-}O)(\mu\text{-}pz)_3Cl_3]$ | 3.269–3.287 | 500 | [30] |
| $[Cu_6(\mu_3\text{-}O)(HV)_3(ClO_4)_7(H_2O)_9]\cdot 8H_2O$ | 3.344 | 247 | [44] |
| $(PPN)_3[Cu_3(\mu_3\text{-}O)_{0.78}(\mu_3\text{-}OH)_{0.22}(\mu_3\text{-}Cl)_{0.22}(\mu_3\text{-}Clpz)_3Cl_3]\cdot H_2O\cdot Cl$ | 3.272 | 49.8 | [45] |
| $[Cu_3(\mu_3\text{-}OH)(daat)(Hdat)_2(ClO_4)_2(H_2O)_3](ClO_4)_2\cdot 2H_2O$ | 3.305–3.410 | 177 | [36] |
| $[Cu_3(\mu_3\text{-}OH)(aaat)_3(H_2O)_3](ClO_4)_2\cdot 3H_2O$ | 3.361–3.389 | 178 | [36] |

aat = 3-acetylamino-1,2,4-triazolate; pz = pyrazolate; trz = triazolate; HV = 5-amino-3-picolinamido-1,2,4-triazole; daat = 3,5-diacetylamino-1,2,4-triazolate; Hdat = 3,5-diamino-1,2,4-triazole; aaat = 3-acetylamino-5-amino-1,2,4-triazolate

## 4. Conclusions

We have demonstrated an efficient gram-scale synthesis of the ligand H-dmta and have extended the family of triazole MOFs with a new thermally and solvolytically stable family member. The coordination of copper ions in this MOF is revealed to be completely distinct from that observed in other triazole MOF derivatives through the analysis of single-crystal X-ray diffraction data. In our case, it crystalizes in the chiral cubic Crystal System $P2_13$. Here the copper ions span two triangles whose edges are connected by triazoles and in the middle of the triangle are connected either by an OXO or HYDROXO, which has been further verified by IR-spectroscopy. This triangle arrangement is known for its magnetic properties and was therefore investigated with ESR and SQUID in addition to the classical characterization methods. Unfortunately, this MOF is ESR silent in the X-band from 4 to 300 K therefore only the SQUID data could be used. The SQUID data was analysed using an isotropic and antisymmetric exchange Hamiltonian with a Zeeman term for each $[Cu]_3$ triangle ($\widehat{H} = -2\sum_{i=1j>i}^{3} J_1\,\vec{S}_i\vec{S}_j + g^*\mu_B\sum_{i=1}^{6}\vec{S}_i{}^*\vec{H} + G_1\left(\vec{S}_1\times\vec{S}_2 + \vec{S}_2\times\vec{S}_3 + \vec{S}_3\times\vec{S}_1\right)$) and one isotropic exchange between the triangles. The resulting strong antiferromagnetic and antisymmetric exchange parameters demonstrate that the rigid ligand backbone impedes any distortions and prevents the system from lifting the degeneracy by lowering the symmetry. Consequently, our framework is a promising candidate for spintronic applications as Qubits.

### CRediT authorship contribution statement

**Marcel Hirrle:** Investigation. **Richard Röß-Ohlenroth:** Investigation. **Tobias Luxenhofer:** Investigation. **Björn Bredenkötter:** Investigation. **Maryana Kraft:** Investigation. **Hans-Albrecht Krug von Nidda:** Investigation. **Dirk Volkmer:** Supervision.

## Declaration of competing interest

The authors declare that they have no known competing financial interests or personal relationships that could have appeared to influence the work reported in this paper.

## Appendix A. Supplementary data

Supplementary data to this article can be found online at https://doi.org/10.1016/j.jssc.2025.125328.

## Data availability

I have shared my data at the attached file step

## References


[1] A.E. Thorarinsdottir, T.D. Harris, Chem. Rev. 120 (2020) 8716, https://doi.org/10.1021/acs.chemrev.9b00666.
[2] C. Yang, R. Dong, M. Wang, P.S. Petkov, Z. Zhang, M. Wang, P. Han, M. Ballabio, S. A. Bräuninger, Z. Liao, et al., Nat. Commun. 10 (2019) 3260, https://doi.org/10.1038/s41467-019-11267-w.
[3] X. Zhao, S. Liu, Z. Tang, H. Niu, Y. Cai, W. Meng, F. Wu, J.P. Giesy, Sci. Rep. 5 (2015) 11849, https://doi.org/10.1038/srep11849.
[4] R. Dong, Z. Zhang, D.C. Tranca, S. Zhou, M. Wang, P. Adler, Z. Liao, F. Liu, Y. Sun, W. Shi, et al., Nat. Commun. 9 (2018) 2637, https://doi.org/10.1038/s41467-018-05141-4.
[5] M.-H. Zeng, Z. Yin, Y.-X. Tan, W.-X. Zhang, Y.-P. He, M. Kurmoo, J. Am. Chem. Soc. 136 (2014) 4680, https://doi.org/10.1021/ja500191r.
[6] J.F. Nossa, M.F. Islam, M.R. Pederson, C.M. Canali, Phys. Rev. B 107 (2023), https://doi.org/10.1103/PhysRevB.107.245402.
[7] B. Kintzel, M. Böhme, J. Liu, A. Burkhardt, J. Mrozek, A. Buchholz, A. Ardavan, W. Plass, Chemical communications (Cambridge, England) 54 (2018) 12934, https://doi.org/10.1039/C8CC06741D.
[8] K.-B. Wang, Q. Xun, Q. Zhang, EnergyChem 2 (2020) 100025, https://doi.org/10.1016/j.enchem.2019.100025.
[9] K. Wang, Y. Guo, Q. Zhang, Small Structur. 3 (2022), https://doi.org/10.1002/sstr.202100115.
[10] K. Wang, C. Chen, Y. Li, Y. Hong, H. Wu, C. Zhang, Q. Zhang, Small (Weinheim an der Bergstrasse, Germany) 19 (2023) e2300054, https://doi.org/10.1002/smll.202300054.
[11] S. Biswas, M. Tonigold, M. Speldrich, P. Kögerler, M. Weil, D. Volkmer, Inorg. Chem. 49 (2010) 7424, https://doi.org/10.1021/ic100749k.
[12] M. Grzywa, D. Denysenko, J. Hanss, E.-W. Scheidt, W. Scherer, M. Weil, D. Volkmer, Dalton Trans. 41 (2012) 4239, https://doi.org/10.1039/C2DT12311H.
[13] T.W. Werner, S. Reschke, H. Bunzen, H.-A.K. von Nidda, J. Deisenhofer, A. Loidl, D. Volkmer, Inorg. Chem. 55 (2016) 1053, https://doi.org/10.1021/acs.inorgchem.5b01982.
[14] M. Grzywa, R. Röß-Ohlenroth, C. Muschielok, H. Oberhofer, A. Błachowski, J. Żukrowski, D. Vieweg, H.-A.K. von Nidda, D. Volkmer, Inorg. Chem. 59 (2020) 10501, https://doi.org/10.1021/acs.inorgchem.0c00814.
[15] J.G. Park, B.A. Collins, L.E. Darago, T. Runčevski, M.E. Ziebel, M.L. Aubrey, H.Z. H. Jiang, E. Velasquez, M.A. Green, J.D. Goodpaster, et al., Nat. Chem. 13 (2021) 594, https://doi.org/10.1038/s41557-021-00666-6.
[16] M.-A. Bouammali, N. Suaud, N. Guihéry, R. Maurice, Inorg. Chem. 61 (2022) 12138, https://doi.org/10.1021/acs.inorgchem.2c00939.
[17] I. Dzyaloshinsky, J. Phys. Chem. Solid. 4 (1958) 241, https://doi.org/10.1016/0022-3697(58)90076-3.
[18] T. Moriya, Phys. Rev. 120 (1960) 91, https://doi.org/10.1103/PhysRev.120.91.
[19] F. Rouquerol, Adsorption by powders and porous solids, in: Principles, Methodology and Applications, Academic Press, Kidlington, Oxford, 2014.
[20] a) J. Jagiello, M. Thommes, Carbon 42 (2004) 1227, https://doi.org/10.1016/j.carbon.2004.01.022;
b) P.I. Ravikovitch, A.V. Neimark, Colloids Surf., A 187–188 (2001) 11, https://doi.org/10.1016/S0927-7757(01)00614-8.
[21] Bruker, APEX4, Bruker.
[22] Saint Madison, Bruker Analytical X-Ray Systems, INC., 2021.
[23] L. Krause, R. Herbst-Irmer, G.M. Sheldrick, D. Stalke, J. Appl. Crystallogr. 48 (2015) 3, https://doi.org/10.1107/S1600576714022985.
[24] Sheldrick, SHELXL-2019/1 (2019).
[25] A.L. Spek, Acta Crystallogr. D 65 (2009) 148, https://doi.org/10.1107/S090744490804362X.
[26] C.-H. Tsai, W.-C. Huang, W.-S. Wang, C.-J. Shih, W.-F. Chi, Y.-C. Hu, Y.-H. Yu, J. Colloid Interface Sci. 495 (2017) 111, https://doi.org/10.1016/j.jcis.2017.02.002.
[27] S. Hauptmann, H. Wilde, K. Moser, J. Prakt, Chem 313 (1971) 882, https://doi.org/10.1002/prac.19713130513.
[28] H.V. Pechmann, W. Bauer, Ber. Dtsch. Chem. Ges. 42 (1909) 659, https://doi.org/10.1002/cber.190904201104.
[29] M. Grzywa, C. Geßner, D. Denysenko, B. Bredenkötter, F. Gschwind, K.M. Fromm, W. Nitek, E. Klemm, D. Volkmer, Dalton Trans. 42 (2013) 6909, https://doi.org/10.1039/C3DT32302A.
[30] P.A. Angaridis, P. Baran, R. Boca, F. Cervantes-Lee, W. Haase, G. Mezei, R. G. Raptis, R. Werner, Inorg. Chem. 41 (2002) 2219, https://doi.org/10.1021/ic010670l.
[31] M. Rivera-Carrillo, I. Chakraborty, G. Mezei, R.D. Webster, R.G. Raptis, Inorg. Chem. 47 (2008) 7644, https://doi.org/10.1021/ic800531y.
[32] A. Abragam, B. Bleaney, Electron Paramagnetic Resonance of Transition Ions, Oxford Univ. Press, Oxford, 2013.
[33] A. Shengelaya, H. Keller, K.A. Müller, B.I. Kochelaev, K. Conder, Phys. rev. B, Condens. matter 63 (2001), https://doi.org/10.1103/PhysRevB.63.144513.
[34] K.A. Müller, J. Phys. Condens. Matter 19 (2007) 251002, https://doi.org/10.1088/0953-8984/19/25/251002.
[35] N.F. Chilton, R.P. Anderson, L.D. Turner, A. Soncini, K.S. Murray, J. Comput. Chem. 34 (2013) 1164, https://doi.org/10.1002/jcc.23234.
[36] S. Ferrer, F. Lloret, E. Pardo, J.M. Clemente-Juan, M. Liu-González, S. García-Granda, Inorg. Chem. 51 (2012) 985, https://doi.org/10.1021/ic2020034.
[37] R. HassanAbadi, R.M. Eremina, M. Hemmida, A. Dittl, M.V. Eremin, B. Wolf, W. Assmus, A. Loidl, H.-A. Krug von Nidda, Phys. Rev. B 103 (2021), https://doi.org/10.1103/PhysRevB.103.064420.
[38] M.A. Fayzullin, R.M. Eremina, M.V. Eremin, A. Dittl, N. van Well, F. Ritter, W. Assmus, J. Deisenhofer, H.-A.K. von Nidda, A. Loidl, Phys. Rev. B 88 (2013), https://doi.org/10.1103/PhysRevB.88.174421.
[39] K.Y. Povarov, A.I. Smirnov, O.A. Starykh, S.V. Petrov, A.Y. Shapiro, Phys. Rev. Lett. 107 (2011) 37204, https://doi.org/10.1103/PhysRevLett.107.037204.
[40] S. Ferrer, J.G. Haasnoot, J. Reedijk, E. Müller, M.B. Cingi, M. Lanfranchi, A. M. Lanfredi, J. Ribas, Inorg. Chem. 39 (2000) 1859, https://doi.org/10.1021/ic981393u.
[41] W. Ouellette, A.V. Prosvirin, V. Chieffo, K.R. Dunbar, B. Hudson, J. Zubieta, Inorg. Chem. 45 (2006) 9346, https://doi.org/10.1021/ic061102e.
[42] S. Ferrer, F. Lloret, I. Bertomeu, G. Alzuet, J. Borrás, S. García-Granda, M. Liu-González, J.G. Haasnoot, Inorg. Chem. 41 (2002) 5821, https://doi.org/10.1021/ic020179+.
[43] L.-L. Zheng, J.-D. Leng, S.-L. Zheng, Y.-C. Zhaxi, W.-X. Zhang, M.-L. Tong, CrystEngComm 10 (2008) 1467, https://doi.org/10.1039/b806202a.
[44] S. Ferrer, J. Hernández-Gil, F.J. Valverde-Muñoz, F. Lloret, A. Castiñeiras, RSC Adv. 9 (2019) 29357, https://doi.org/10.1039/C9RA05922A.
[45] L. Mathivathanan, Y. Sanakis, R.G. Raptis, P. Turek, A.K. Boudalis, Physical chemistry chemical physics : PCCP 23 (2021) 14415, https://doi.org/10.1039/d1cp01965a.
[46] F. Zhang, X. Li, Y. Wu, X. Wang, J. Zhao, W. Gao, Phys. Rev. B 106 (2022), https://doi.org/10.1103/PhysRevB.106.L100407.
[47] R. Röß-Ohlenroth, M. Hirrle, M. Kraft, A. Kalytta-Mewes, A. Jesche, H.-A. Krug von Nidda, D. Volkmer, Zeitschrift anorg allge chemie (2022) 648. https://doi.org/10.1002/zaac.202200153.